*J. Fluid Mech.* (2014), *vol.* 741, *pp* 350–376. © Cambridge University Press 2014 
doi:10.1017/jfm.2013.672

# Flow of a falling liquid curtain into a pool

**Harumichi Kyotoh[1,†], Kazuki Fujita[2], Koichi Nakano[3] and Takeaki Tsuda**

[1]Department of Engineering Mechanics and Systems, University of Tsukuba, Tsukuba, Ibaraki 302-8573, Japan

[2]Research and Development Department, Yuken Kogyo Co., Ltd, Ayase, Kanagawa 252-1113, Japan

[3]Technology Development Center, Dai Nippon Printing Co., Ltd., Tsukuba, Ibaraki 300-2646, Japan

(Received 3 February 2013; revised 6 November 2013; accepted 16 December 2013; first published online 17 February 2014)

We investigate the low-Weber-number flow of a liquid curtain bridged between two vertical edge guides and a pool surface. Three flow patterns, namely, steady vertical flow, steady oblique flow, and oscillatory oblique flow, are observed in our experiment. These patterns are caused by the Coanda effect of the jet around the meniscus that is formed in the matching region common to the liquid curtain and the pool surface. Here, the deflection angle of the jet is greater than 90°. The equation describing the motion of the liquid curtain applicable for a finite curtain slope is obtained using the intrinsic coordinate system in which the distance along the curtain is selected as one of the coordinates, and the equation of the meniscus motion is derived by considering the conservation of momentum. The curtain deformations of oblique flows are analysed by generating numerical simulations of these equations, and the simulation results are then compared with experimental results. Also, the period of oscillatory oblique flow is discussed and explained via the response analyses of the curtain, and the result shows that the period of the oscillations is close to that of the most amplified mode of the liquid curtain. Further, the detachment angle of the jet is discussed in relation to the Coanda effect of the jet in the meniscus.

**Key words:** interfacial flows (free surface), jets, liquid bridges

## 1. Introduction

Curtain coating can be applied to coat thin liquid layers on irregular surfaces with very high coating speeds (Kistler & Schweizer 1997). This method has been applied only for liquid curtains with a high Weber number, i.e. $We > 2$, for which the inertial force is greater than the surface tension. In the present paper, $We$ is defined by $\rho q V/\gamma$ where $\rho$ denotes the liquid density, $q$ the unit discharge, $V$ the liquid velocity, and $\gamma$ the surface tension. Therefore, to explore new possibilities in curtain coating, we examine the flow of a falling liquid curtain with a low Weber number, $We < 2$, to be used to coat irregular surfaces; in particular, we focus on a low-viscosity liquid with thin liquid layers. Before studying the curtain coating applied to a substrate, we investigate the flow of a falling liquid curtain into a liquid surface.

Falling film flows on a rising vertical wall exhibit various flow regimes such as rising film, obstructed rising film, poured falling film and falling film regimes

† Email address for correspondence: kyotoh@kz.tsukuba.ac.jp

https://doi.org/10.1017/jfm.2013.672 Published online by Cambridge University Press

(Kheshgi, Kistler & Scriven 1992). A round jet falling into a pool exhibits three regimes, i.e. spreading, spreading with a blob, and a jet (Sebilleau, Limat & Eggers 2009), and it has been concluded that the flow regimes are not sensitive to surface contamination and depend only on the flow Reynolds number. The phenomenon of a liquid curtain falling into a pool has previously been studied and it was found that there are three observable flow regimes, i.e. steady vertical flow, steady oblique flow, and oscillatory oblique flow (Kyotoh *et al.* 2009; Takagi 2010, see also the relevant movie ('MovieIntroSlow' is available online at http://dx.doi.org/10.1017/jfm.2013.672): the movie shows that the liquid curtain oscillates in a pool when the falling height is small, but the oscillations stop abruptly after the falling height exceeds a given threshold. Here, unit discharge is kept constant, and hence, the Reynolds number remains constant during the experiment). Hence, the present experimental results contradict the conclusion drawn by Sebilleau *et al.* (2009). The jet from the curtain is bent by the meniscus, and this event propagates into the curtain upstream, thereby affecting the behaviour of the liquid curtain. However, these flow mechanisms have not been studied in detail thus far. Explaining these phenomena is difficult partly because the flow is fully two-dimensional owing to the existence of the meniscus.

The deflection of the jet around a convex body surface is known as the Coanda effect (Newman 1961). In this phenomenon, a jet flows over the convex body surface without separation. Therefore, without using the term 'Coanda effect', the study can be understood as focusing on the separation of a jet from a body surface in general (Neuendorf & Wygnanski 1999). The target of the present study is to examine the flow of a jet along a curved free surface, that is, the Coanda effect of the jet in the meniscus.

The large-amplitude unsteady motion of the liquid curtain is investigated in the present study, since the liquid begins to fall vertically at the slot exit and flows nearly tangentially at the pool surface. Ida (1995), van de Fliert, Howell & Ockendon (1995) and Ida & Miksis (1998) derived the equation of motion of such a curtain in the frame of reference taken along the curtain. For a quasi-steady flow, Kistler et al. derived the momentum equation integrated across the curtain in the transverse direction (Higgins & Scriven 1979; Kistler 1984). For a steady flow, the curtain profile under a large deformation is adequately described by the curtain equations derived under a uniform velocity distribution in the curtain (Finnicum, Weinstein & Ruschak 1993). For an unsteady flow, a model taking into account the local inertial force has been derived by Weinstein *et al.* (1997) and Weinstein, Hoff & Ross (1998). We derive simplified equations describing the large-amplitude motions of the liquid curtain based on the methods suggested by van de Fliert *et al.* (1995), Ida (1995), Yao & Stewart (1996) and Ida & Miksis (1998), and we use the methods introduced by Higgins & Scriven (1979).

The drag force on the liquid curtain is dominated by the flow in the meniscus. Observing the flow from a coordinate system moving at the same speed as the meniscus, the jet from the liquid curtain impinges into the cross-flow of the pool. Hence, studies on the flow characteristics of jets in cross-flow are relevant to determine the drag force on the jet from the liquid curtain in the following discussion. Haniu & Ramaprian (1989) measured the trajectories of two-dimensional jets in cross-flow and found that the trajectory is scaled by a momentum length scale defined as the ratio of the jet momentum flux to the cross-flow momentum. Fric & Roshko (1994) showed that the vortical structures formed in the wake of a jet in cross-flow are quite different from those for a solid body. In particular, in the soap-film flow around a jet of water, no wake vortices or structures are observed

https://doi.org/10.1017/jfm.2013.672 Published online by Cambridge University Press

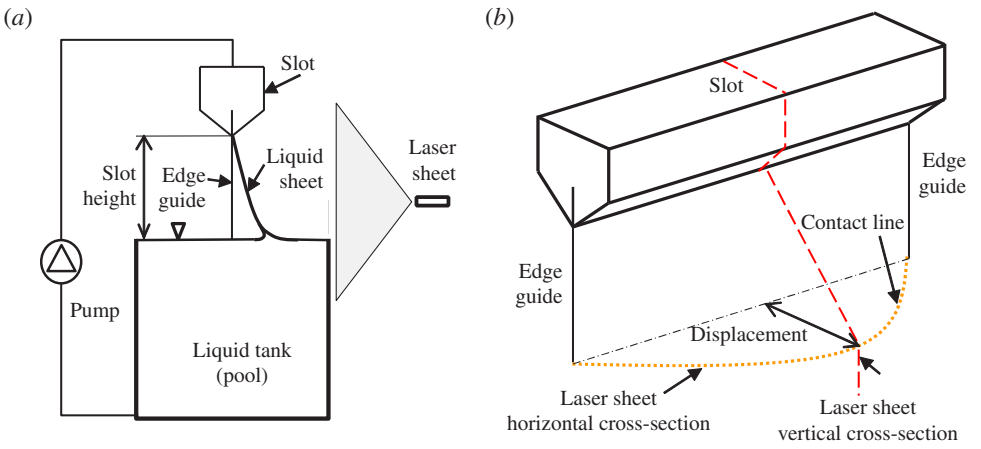



FIGURE 1. (Colour online) Experimental setup. (*a*) Experimental apparatus. (*b*) Flow visualization.

downstream of the jet (Fric & Gharib 1990). Therefore, the drag force exerted on the jet in the meniscus is considered to be different from that of a solid body.

In the present study, three flow regimes observed in a liquid curtain falling into a pool are investigated by flow visualizations and the modelling of these flows. In § 2, we describe how a flow is made easily visible to the eye by mixing nylon particles into the selected liquid, and how the velocity fields in the pool are measured using particle image velocimetry (PIV). These experiments show that the transition among the flow regimes is caused by a change in flow patterns in the pool. In § 3, a new equation describing the motion of a liquid curtain is derived without any restriction on the curtain slope, and the momentum conservation law is applied for the flow around the meniscus formed between the curtain and the pool to obtain a dynamic model of the meniscus motion. In § 4, the equations of the curtain and meniscus motions are coupled and solved numerically. In § 5, the period and amplitude of oscillatory oblique flow are analysed based on the model derived in § 3, and the flow deflection in the meniscus is discussed on the basis of the Coanda effect. Finally, in § 6, we discuss future studies planned for further investigations in this direction.

## 2. Experiment

Figure 1(*a*) shows the experimental setup used in the present study. Liquid is circulated from a tank to a slot through a diaphragm pump (TACMINA TPL2M-028). This pump has a structure such that the motor and pump are connected through Teflon resin to suppress heat conduction, so that the rise in the liquid temperature is negligible during our experiment. Two vertical edge guides are installed in the two corners of the slot and a liquid curtain forms a bridge between these guides. The edge guides are composed of stainless steel, and each guide has an outer diameter of 0.5 mm.

The curtain thus forms between the exit of the slot and the liquid tank (pool) surface. As shown in figure 1(*b*), both the curtain profile and liquid flow are visualized by a laser sheet over the liquid curtain (green laser FKLA5000) and obtaining pictures using a high-speed camera (Photron Fastcam SA4).

https://doi.org/10.1017/jfm.2013.672 Published online by Cambridge University Press

| | | | |
|---|---|---|---|
| Die width $b$ (cm) | | 12.5 | |
| Slot width $H_0$ (μm) | | 100 | |
| Unit discharge $q$ ($cm^2\ s^{-1}$) | | 0.32 to 1.36 | |
| Liquid temperature (°C) | | 26 | |
| Water:ethanol:glycerin (wt %) | 95:5:10 | 70:0:30 | 90:0:10 |
| Viscosity $\mu$ (cP) | 1.03 | 1.25 | 2.5 |
| Surface tension coefficient $\gamma$ (N $m^{-1}$) | 57 | 65 | 73 |
| Density $\rho$ (g $cm^{-3}$) | 0.98 | 1.02 | 1.08 |

TABLE 1. Experimental conditions for the classification of flow patterns described in § 2.1.

### 2.1. *Visualization of a liquid curtain*

Table 1 lists the liquid properties and the experimental conditions in our study, which aid in classifying the observed flow patterns. The liquid is prepared by mixing water, ethanol, and glycerin in three appropriate ratios in order to vary the liquid viscosity and surface tension over a broad range. The die width is 12.5 cm, the exit slot width is 100 μm, and the acrylic tank has physical dimensions of 14.8 cm width, 8.0 cm length, and 11.0 cm depth.

Figure 2 depicts the following flow patterns observed in the present study.

(*a*) Steady vertical flow: the curtain profile is vertical, and the flow of the curtain vertically impinges on the pool. The meniscus develops from the pool surface to the curtain.

(*b*) Steady oblique flow: the curtain profile is oblique and the flow of the curtain deflects in the horizontal direction at the pool surface. The meniscus develops from the pool surface to the curtain.

(*c*) Oscillating oblique flow: the curtain profile is oblique and oscillates periodically back and forth. The meniscus develops from the pool surface to the curtain. Flow patterns ① → ④ depend on the angle $\theta_S$ which is the angle of the liquid curtain to the pool surface along the vertically downward direction. Here, $\theta_{det}$ denotes the detachment angle at which the flow of the curtain detaches from the meniscus surface, and $\theta_{ata}$ denotes the attachment angle at which the flow of the curtain attaches to the meniscus surface.

(*d*) Vertical jet: the curtain profile is vertical and the flow impinges vertically on the pool. No meniscus is developed from the pool surface to the curtain.

Figure 3 shows the classification of these flows in the $We_S$–$Re$ plane. Here, $We_S$ denotes the Weber number at the liquid surface of the pool, and $Re$ denotes the Reynolds number; they are respectively defined as

$$We_S = \frac{\rho q V_S}{\gamma}, \quad Re = \frac{\rho q}{\mu}. \tag{2.1}$$

Here, $\rho$ denotes the liquid density, $\gamma$ the surface tension coefficient, $\mu$ the viscosity, and $q$ the unit discharge. The parameter $V_S$ denotes the liquid velocity in the curtain at the pool surface. In the present study, $V_S$ was not measured directly and was estimated from Bernoulli's theorem as follows:

$$V_S = \sqrt{V_I^2 + 2gx_S}, \quad V_I = \sqrt{V_0^2 - 4\left(\frac{4\mu g}{\rho}\right)^{2/3}}, \quad V_0 = \frac{q}{H_0}, \tag{2.2}$$

https://doi.org/10.1017/jfm.2013.672 Published online by Cambridge University Press

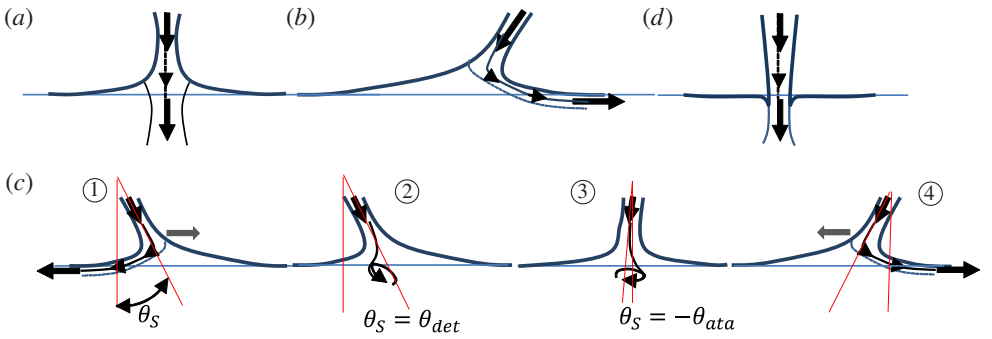



FIGURE 2. (Colour online) Flow patterns observed in the experiment of a falling liquid curtain into a pool. (*a*) Steady vertical flow. (*b*) Steady oblique flow. (*c*) Oscillatory oblique flow: ① to ④ depict the flow changes over time. (*d*) Vertical jet.

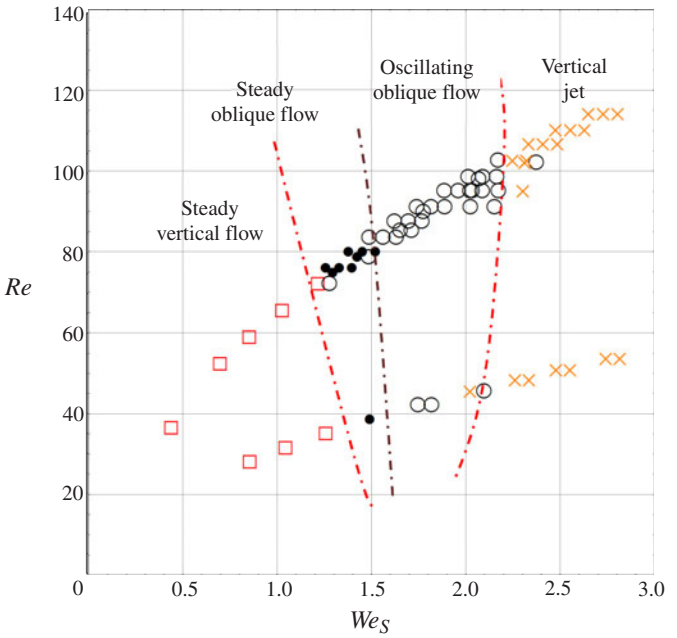



FIGURE 3. (Colour online) Classification of the flow observed in the present experiment. Flow patterns shown here are schematically described in figure 2. See also the relevant movie in the introduction.

where $H_0$ denotes the slot width, $x_S$ the distance between the slot exit and the pool surface (slot height), $g$ the gravitational acceleration, $V_I$ the liquid velocity at the slot exit corrected by considering the viscosity of the liquid, and $V_0$ the mean velocity of the liquid at the slot exit. In the following sections, the subscript '$S$' denotes the value of the indicated parameter at the pool surface. The effect of viscosity on the liquid flow in the curtain is evaluated by using the formula $8g\mu/\rho V_I^3$ (Weinstein *et al.* 1997, for instance). The value is around 0.003 at the slot exit, and hence, the effect of viscosity is negligible in the present study.

The flows are roughly classified simply using $We_S$, i.e. (*a*) steady vertical flow for $We_S \leqslant 1.2$, (*b*) steady oblique flow for $1.2 \leqslant We_S \leqslant 1.6$, (*c*) oscillating oblique flow

https://doi.org/10.1017/jfm.2013.672 Published online by Cambridge University Press

| | |
|---|---|
| Die width $b$ (cm) | 6.0 |
| Slot width $H_0$(μm) | 300 |
| Liquid temperature (°C) | 25 |
| Water:ethanol:glycerin (wt %) | 76:4:20 |
| Viscosity $\mu$ ($cP$) | 1.9 |
| Surface tension coefficient $\gamma$ (N m$^{-1}$) | 52 |
| Density $\rho$ (g cm$^{-3}$) | 1.04 |

TABLE 2. Experimental conditions for flow visualizations in § 2.2.

for $1.6 \leqslant We_S \leqslant 2.2$, and ($d$) vertical jet for $We_S \geqslant 2.2$. However, the region of the oblique flow shrinks as $Re$ reduces. It is to be noted that the Reynolds number $Re$ is constant in the downstream direction of the liquid curtain.

### 2.2. *Visualization of the curtain, meniscus, and flow in the pool*

To clarify the mechanism causing the occurrence of oblique flows, 0.04 wt % nylon particles (Diamid 2157 manufactured in Degussa, mean diameter 57 μm, density 1.02 g cm$^{-3}$) are mixed with the liquid, and the vertical cross-section of the curtain including the meniscus and the pool, is visualized by a laser sheet as shown in figure 1($b$). Because the camera is focused on the cross-section of the laser sheet, the edge guide is not clearly seen in the image, and as a result, the edge guide does not distort the image of the vertical cross-section of the liquid curtain.

The experimental conditions for this case are listed in table 2. In the experimental trials discussed, we have observed only the basic mode of curtain deformation, which is symmetric with respect to the vertical plane located midway between the two edge guides.

#### 2.2.1. *Steady oblique flow*

Figure 4 shows the particle paths under steady oblique flow. In figures 4 and 5, there is a blurred area at the pool surface, at the location of the edge guide and the meniscus around it. The images in figure 4 are prepared by the superimposition of 10 successive images recorded by a high-speed camera at 2000 f.p.s. The path of the nylon particles indicates the flow direction and velocity. The broken line indicates the trajectory of the nylon particles flowing along the left-hand surface of the meniscus, which are subsequently jetted to the right-hand surface layer of the pool. The pressure gradient along the horizontal direction caused by the difference between the curvatures of the left- and right-hand menisci accelerates the fluid particles towards the right.

Table 3 lists the experimental conditions and results for a steady oblique flow. The jet velocity $V_{Sout}$ is measured via PIV, as shown in figure 4. The magnitude of $V_{Sout}$ is around 0.2 to 0.3 times the liquid velocity $V_S$. The reason for this reduction in flow velocity is considered to be a momentum loss due to the bending of the jet and its penetration of the meniscus. The horizontal displacement of the meniscus from the pool surface located immediately under the slot is denoted by $A_{ex}$, the amplitude of the meniscus displacement. We discuss the relation between the value of $A_{ex}$ and the velocity ratio $V_{Sout}/V_S$ later in § 5.2.

#### 2.2.2. *Oscillatory oblique flow*

Figure 5 shows a time-series of images of the oscillatory oblique flow at the vertical cross-section of the curtain, as shown in figure 1($b$). Each figure is obtained by the

https://doi.org/10.1017/jfm.2013.672 Published online by Cambridge University Press

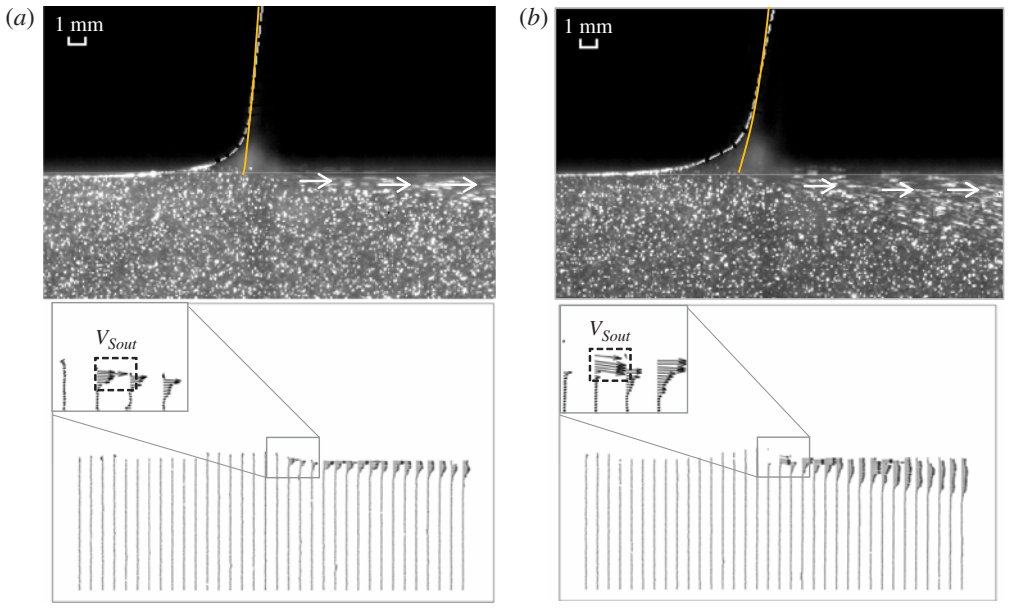



FIGURE 4. (Colour online) Steady oblique flow for (*a*) $q = 0.623$ cm$^2$ s$^{-1}$ and (*b*) $q = 0.751$ cm$^2$ s$^{-1}$. The experimental conditions for these cases are listed in table 3. Broken and solid lines in the visualizations in the upper figures indicate the particle path in the experiment and the curtain profile calculated in § 4.1 respectively. Arrows indicate the flow direction. The lower figures show velocity vectors obtained from PIV. The term $V_{Sout}$ denotes the jet velocity in the neighbourhood of the meniscus. See also movie 1 for (*a*) and movie 2 for (*b*). See Movies 1 and 2 available online at http://dx.doi.org/10.1017/jfm.2013.672

| | | | | | | | | |
|---|---|---|---|---|---|---|---|---|
| Unit discharge $q$ (cm$^2$ s$^{-1}$) | 0.496 | 0.623* | 0.751* | 0.878 | 1.01 | 1.13 | 1.13 | 1.26 |
| Slot height $x_S$ (cm) | 2.0 | 2.0 | 2.0 | 2.0 | 2.0 | 1.0 | 1.5 | 1.0 |
| Amplitude $A_{ex}$ (mm) | 1.0 | 1.9 | 3.5 | 5.1 | 5.1 | 5.0 | 7.8 | 6.5 |
| Jet velocity $V_{Sout}$ (cm s$^{-1}$) | 9.6 | 12.9 | 19.0 | 19.0 | 14.1 | 15.6 | 22.0 | 11.6 |
| Liquid velocity $V_S$ (cm s$^{-1}$) | 64.8 | 66.0 | 67.4 | 69.1 | 71.0 | 57.6 | 65.5 | 60.5 |
| Velocity ratio $V_{Sout}/V_S \equiv \chi_{ex}$ | 0.15 | 0.20 | 0.28 | 0.27 | 0.20 | 0.27 | 0.34 | 0.19 |

TABLE 3. Experimental conditions pertaining to a steady oblique flow. Here, the jet velocity $V_{Sout}$ is measured at the right-hand edge of the meniscus, and $V_S$ denotes the liquid velocity in the curtain at the pool surface, which is estimated from (2.2). See figure 4 for experiments relevant to the entries 0.623* and 0.751*.

superimposition of 10 successive images recorded by the high-speed camera at 2000 f.p.s., so that the flow direction and velocity can be observed from the path of the nylon particles. A schematic of the curtain and the flow near the meniscus are shown in figure 2(*c*). The displacement of the meniscus increases while the Coanda effect is operative, and subsequently, the meniscus displacement decreases when the Coanda effect disappears. As a result, the oscillatory motion of the meniscus continues as illustrated in figure 2(*c*).

https://doi.org/10.1017/jfm.2013.672 Published online by Cambridge University Press

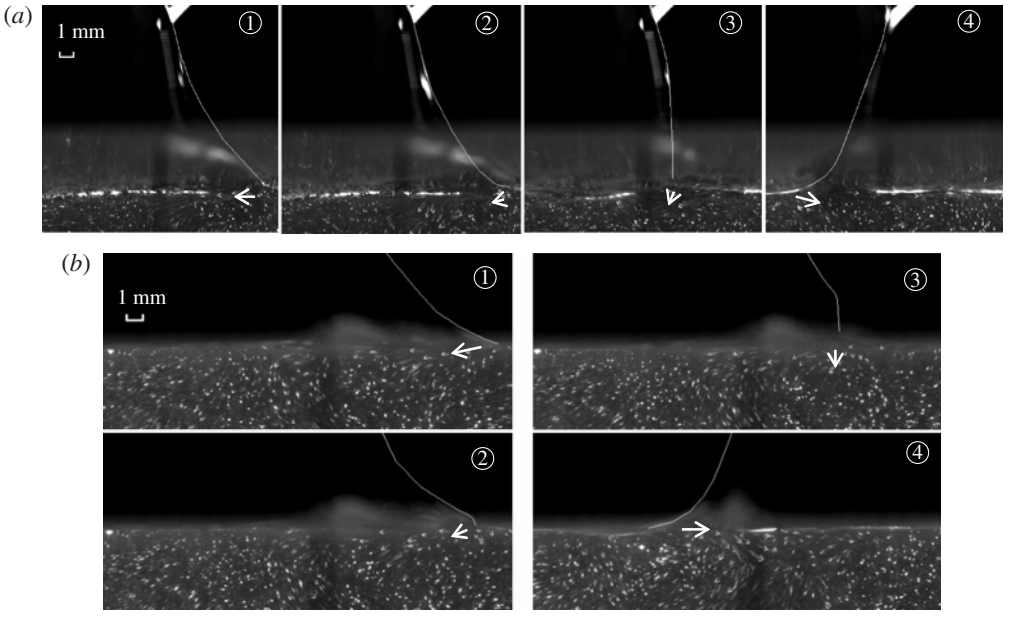



FIGURE 5. Visualizations of oscillatory oblique flow for (*a*) $q = 1.20$ cm$^2$ s$^{-1}$, $x_S = 1.85$ cm and (*b*) $q = 1.13$ cm$^2$ s$^{-1}$, $x_S = 2.5$ cm. The experimental conditions for these cases are listed in table 4. The curtain profile is traced by the thin white line, and the arrow shows the flow direction. Time increases from ① → ④. These pictures are chosen so that the typical flow patterns are captured. See also movie 3 for (*a*) and movie 4 for (*b*) available online at http://dx.doi.org/10.1017/jfm.2013.672.

| | | | | | | | |
|---|---|---|---|---|---|---|---|
| Unit discharge $q$ (cm$^2$ s$^{-1}$) | 1.01 | 1.13* | 1.13 | 1.13 | 1.13 | 1.20* | 1.26 |
| Slot height $x_S$ (cm) | 4.0 | 2.5 | 3.0 | 3.5 | 4.0 | 1.85 | 2.0 |
| Period $T_{ex}$ (s) | 0.36 | 0.37 | 0.38 | 0.30 | 0.40 | 0.57 | 0.42 |
| Amplitude $A_{ex}$ (mm) | 7.6 | 8.9 | 12.6 | 9.4 | 7.1 | 8.0 | 10.9 |

TABLE 4. Amplitude and period of oscillatory oblique flows. See figure 5 for the experiments relevant to entries 1.13* and 1.20*.

Table 4 lists the amplitude and period of the meniscus in the oscillatory oblique flows for different values of the unit discharge and slot height. The period of oscillations is around 0.4 s. We discuss the period and amplitude later in §§ 5.1 and 5.2.

The displacement of the meniscus as a function of time is shown in figure 6. The broken line denotes the mean slope of the curve around the origin of the ordinate, and the shape of the curve indicates that the time displacement is almost linear, that is, the meniscus is moving at a constant speed. The speed is ∼0.1 times $V_S$ and has the same order as $V_{Sout}$. In the case of $q = 1.20$ cm$^2$ s$^{-1}$ with $x_S = 1.5$ cm, the meniscus of the steady oblique flow began to move, but stopped at the position of the maximum amplitude.

The influence of the boundary layers near the edge guides on the liquid curtain can be considered negligible compared to the bulk deformation of the liquid curtain, since the slot height $x_S$ is less than the width of the die $b$. Moreover, the inertial force of

https://doi.org/10.1017/jfm.2013.672 Published online by Cambridge University Press

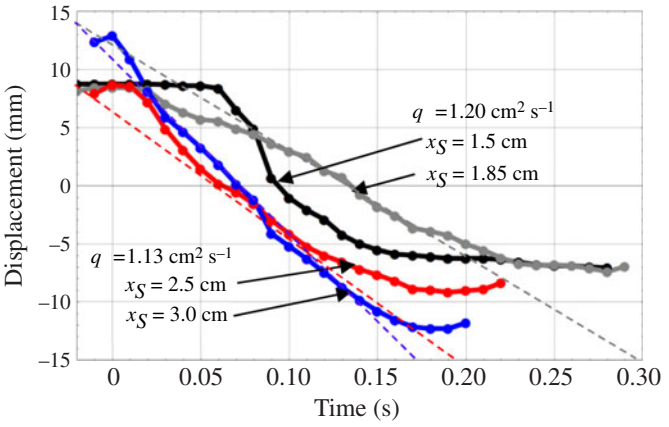



FIGURE 6. (Colour online) Displacements of the meniscus. The origin of the ordinate indicates the position immediately below the slot. The broken lines in the figure denote the mean slopes of the curves drawn manually. As $x_S$ increases, the amplitude of the displacement also increases.

the ambient air flow is also negligible as compared to the inertia force of the liquid curtain because the boundary layer of the air above the liquid curtain surface is very thin for a liquid curtain with a falling height that is as small as ∼2 cm.

## 3. Equations of motion

In this section, we derive the equation for the liquid curtain and the model to describe the meniscus motion in the pool.

### 3.1. *Equations of the liquid curtain*

We derive the governing equation of the liquid curtain when the curtain oscillates with a large amplitude. Here, the curvature of the liquid curtain in the horizontal direction due to the bridging of the liquid curtain to the edge guides is ignored because the width of the die is around three times larger than the falling height of the liquid curtain. Hence, only the liquid curtain in the vertical cross-section is considered in the present study.

#### 3.1.1. *Momentum equation in terms of curvilinear coordinates*

Herein, the viscous stresses in the equation of motion are eliminated because the liquid used has a viscosity similar to water and the Reynolds number is large, i.e. approximately 100.

According to Ida, Miksis and co-workers (for instance, van de Fliert *et al.* 1995; Ida 1995; Yao & Stewart 1996; Ida & Miksis 1998), the centre-curve of the liquid curtain is denoted by $x = X_c(s, \tau)$, $z = Z_c(s, \tau)$, where $s$ denotes the distance along the liquid curtain from the slot exit and $\tau$ denotes time (see figure 7). Moreover, the distance from the centre-curve normal to this curve is denoted by $n$. Hence, the surface of the liquid curtain is designated by $n = \pm H/2$, where $H$ denotes the liquid curtain thickness. The velocity components of the centre-curve along the $s$- and $n$-directions are respectively denoted as $u_c$ and $w_c$, and $\theta$ denotes the angle between the tangential direction of the centre-curve and the vertical direction. These kinematic conditions of

https://doi.org/10.1017/jfm.2013.672 Published online by Cambridge University Press

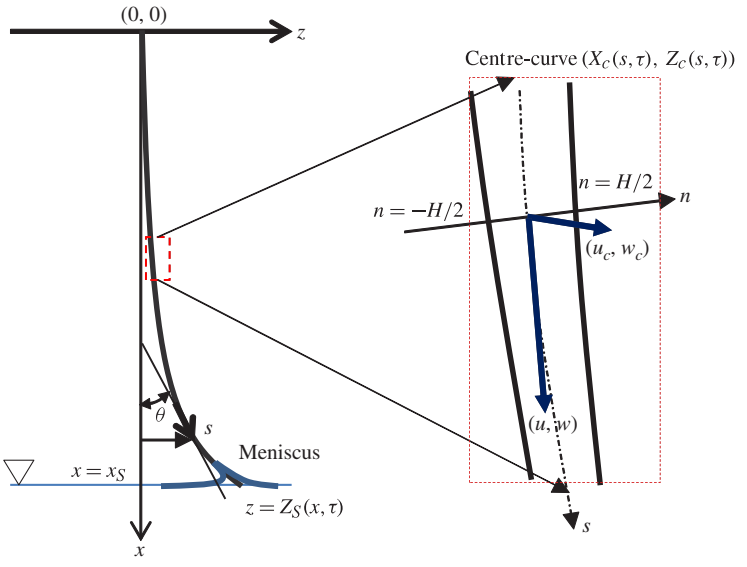



FIGURE 7. (Colour online) Coordinate system for the derivation of the equation describing the motion of the liquid curtain. Here, $(u_c, w_c)$ denotes the centre-curve velocity at the fixed position $s$, and $(u, w)$ denotes the liquid velocity observed from the coordinate system moving with the centre-curve.

the centre-curve are given by

$$\frac{\partial X_c}{\partial s} = \cos\theta, \quad \frac{\partial Z_c}{\partial s} = \sin\theta, \tag{3.1a,b}$$

$$\frac{\partial X_c}{\partial \tau} = u_c\cos\theta - w_c\sin\theta, \quad \frac{\partial Z_c}{\partial \tau} = u_c\sin\theta + w_c\cos\theta. \tag{3.1c,d}$$

Since the flow velocity observed in the inertial coordinates is $(u, w)$, the continuity and Euler equations are respectively expressed as (see (A 6*a*) and A 6*b*) in the Appendix)

$$C_n \equiv \frac{\partial u}{\ell\partial s} + \frac{\partial \ell w}{\ell\partial n} = 0, \tag{3.2a}$$

$$M_s \equiv \rho\left\{\frac{\partial u}{\partial\tau} + (u-u_c)\frac{\partial u}{\ell\partial s} + (w-w_c)\frac{\partial u}{\partial n} - w(u-u_c)\frac{\partial\theta}{\ell\partial s} + \left(n\frac{\partial u}{\ell\partial s} - \frac{w}{\ell}\right)\frac{\partial\theta}{\partial\tau}\right\} - \left(-\frac{\partial p}{\ell\partial s} + \rho g\cos\theta\right) = 0, \tag{3.2b}$$

$$M_n \equiv \rho\left\{\frac{\partial w}{\partial\tau} + (u-u_c)\frac{\partial w}{\ell\partial s} + (w-w_c)\frac{\partial w}{\partial n} + u(u-u_c)\frac{\partial\theta}{\ell\partial s} + \left(n\frac{\partial w}{\ell\partial s} + \frac{u}{\ell}\right)\frac{\partial\theta}{\partial\tau}\right\} - \left(-\frac{\partial p}{\partial n} - \rho g\sin\theta\right) = 0. \tag{3.2c}$$

where $p$ denotes the pressure and $\ell$ indicates the scale factor given as

$$\ell = 1 - n\frac{\partial\theta}{\partial s}. \tag{3.2d}$$

https://doi.org/10.1017/jfm.2013.672 Published online by Cambridge University Press

The integrability conditions of $X_c$ and $Z_c$ from (3.1*a*,*b*) and (3.1*c*,*d*), that is $\partial^2 f/\partial s\partial\tau = \partial^2 f/\partial\tau\partial s$ for $f = X_c$ and $Z_c$, yield the following equations for $u_c$ and $w_c$:

$$\frac{\partial\theta}{\partial s}w_c - \frac{\partial u_c}{\partial s} = 0, \tag{3.3a}$$

$$\frac{\partial\theta}{\partial\tau}w_c - \left(u_c\frac{\partial u_c}{\partial s} + w_c\frac{\partial w_c}{\partial s}\right) = 0, \tag{3.3b}$$

where the integrability conditions have been arranged and solved respectively for $\partial\theta/\partial s$ and $\partial\theta/\partial\tau$. Note that (3.3*a*) and (3.3*b*) yield

$$\frac{\partial\theta}{\partial\tau} = \frac{\partial w_c}{\partial s} + \frac{\partial\theta}{\partial s}u_c, \tag{3.3c}$$

which means that the angular velocity of the centre-curve is represented by its velocity and curvature. In the following, the relative velocity $(u, v)$ defined by

$$u = u - u_c, \quad w = w - w_c, \tag{3.4}$$

is used instead of $(u, w)$ for simplicity of calculations.

The flow velocity of the liquid curtain is assumed to be uniform because the shear stresses from the ambient air are considered negligible in the present study. Therefore, $u$, $w$ and $p$ are expressed as linear functions of $n$ in the following manner:

$$u \approx u(s, \tau), \tag{3.5a}$$

$$w \approx \frac{n + H/2}{H}(w_p - w_m) + w_m, \tag{3.5b}$$

$$p \approx \frac{n + H/2}{H}(p_p - p_m) + p_m, \tag{3.5c}$$

where the subscripts '$p$' and '$m$' on $w$ and $p$ correspond to the values at $n = H/2$ and $n = -H/2$. The velocity and pressure at the free surface are determined from the kinematic and dynamic boundary conditions as follows (see (A 11) in the Appendix):

$$w_p = \frac{\partial}{\partial\tau}\left(\frac{H}{2}\right) + \frac{\partial}{\ell_p\partial s}\left(\frac{H}{2}\right)\left(u + \frac{H}{2}\frac{\partial\theta}{\partial\tau}\right)\bigg|_{n=H/2}, \tag{3.6a}$$

$$w_m = -\frac{\partial}{\partial\tau}\left(\frac{H}{2}\right) - \frac{\partial}{\ell_m\partial s}\left(\frac{H}{2}\right)\left(u - \frac{H}{2}\frac{\partial\theta}{\partial\tau}\right)\bigg|_{n=-H/2}, \tag{3.6b}$$

$$p_p \approx p_a - \gamma\frac{\partial\theta}{\partial s}, \quad p_m \approx p_a + \gamma\frac{\partial\theta}{\partial s}, \tag{3.6c}$$

$$\ell_p \equiv 1 - \frac{H}{2}\frac{\partial\theta}{\partial s}, \quad \ell_m \equiv 1 + \frac{H}{2}\frac{\partial\theta}{\partial s}. \tag{3.6d}$$

Here, $p_a$ denotes the atmospheric pressure, and the curvature at the liquid curtain surfaces is approximated by the curvature of the centre-curve.

According to the method suggested by Higgins & Scriven (1979), the momentum integral equations along the centre-curve are obtained by the substitution of (3.6*a*)–(3.6*c*) into (3.2*a*)–(3.2*c*), by multiplying the scale factor $\ell\,\mathrm{d}n$ with the equations and integrating in the interval $-H/2 \leqslant n \leqslant H/2$. To simplify the model, we assume that the rate of change along the $s$-direction is less than that along the $n$-direction, that the time rate of change is of the order of $u\partial/\partial s$, and that the velocity of the curtain centre-curve is less than the flow velocity in the liquid curtain. The first

https://doi.org/10.1017/jfm.2013.672 Published online by Cambridge University Press

and second assumptions imply that we consider long-wave fluctuations of the liquid curtain, and the third one indicates that the moving speed of the liquid curtain is smaller than the flow velocity in the liquid curtain. These assumptions lead to the following scaling equation:

$$O\left((\partial/\partial s)/(\partial/\partial n)\right)=\epsilon, \quad O\left((u\partial/\partial t)/(\partial/\partial s)\right)=\epsilon, \quad O(u_c/u)=\epsilon, \quad O(w_c/u)=\epsilon, \tag{3.7}$$

where $\epsilon$ denotes a scaling parameter and is set to 1 after applying the perturbation method. By taking into account orders of up to $\epsilon^2$ in the integral equation (3.2*a*)–(3.2*c*), the following simplified equations are obtained:

$$\int_{-H/2}^{H/2} C_n \ell \,\mathrm{d}n \approx \frac{\partial H}{\partial \tau}+u\frac{\partial H}{\partial s}+H\frac{\partial u}{\partial s}+H\left(-\frac{\partial \theta}{\partial s}w_c+\frac{\partial u_c}{\partial s}\right), \tag{3.8a}$$

$$\int_{-H/2}^{H/2} M_s \ell \,\mathrm{d}n \approx \rho H\left\{\frac{\partial}{\partial \tau}(u+u_c)+u\frac{\partial u}{\partial s}+u\left(-\frac{\partial \theta}{\partial s}w_c+\frac{\partial u_c}{\partial s}\right)\right\}-\rho g H\cos\theta, \tag{3.8b}$$

$$\int_{-H/2}^{H/2} M_n \ell \,\mathrm{d}n \approx \rho H\left(\frac{\partial w_c}{\partial \tau}+u\frac{\partial w_c}{\partial s}+\frac{\partial \theta}{\partial \tau}u\right)+\frac{\partial \theta}{\partial s}\left\{\rho H u(u+u_c)-2\gamma\right\}+\rho g H\sin\theta. \tag{3.8c}$$

Setting the above integrals to 0, the governing equations for the unknowns $H$, $u$, $\theta$, $u_c$ and $w_c$ are obtained. Considering (3.3*a*) and (3.3*c*), (3.8*a*)–(3.8*c*) can be reduced to

$$\frac{\partial H}{\partial \tau}+u\frac{\partial H}{\partial s}+H\frac{\partial u}{\partial s}=0, \tag{3.9a}$$

$$\frac{\partial}{\partial \tau}(u+u_c)+u\frac{\partial u}{\partial s}-g\cos\theta=0, \tag{3.9b}$$

$$\frac{\partial w_c}{\partial \tau}+2u\frac{\partial w_c}{\partial s}+\frac{\partial \theta}{\partial s}\left\{u(u+2u_c)-\frac{2\gamma}{\rho H}\right\}+g\sin\theta=0. \tag{3.9c}$$

The above equations can be solved under the boundary conditions at $s=0$ and $s=s_S$ as follows:

$$Z_c(0,\tau)=0, \quad H(0,\tau)=H_I, \quad u(0,\tau)=V_I, \quad u_c(0,\tau)=0, \quad w_c(0,\tau)=0, \tag{3.10a}$$

$$Z_c(s_S,\tau)=Z_M(\tau), \tag{3.10b}$$

where $s_S$ satisfies $X_c(s_S,\tau)=x_S$ and $Z_M$ denotes the displacement of the meniscus at the pool surface.

### 3.1.2. *Momentum equation in terms of the vertical coordinate*

To obtain the boundary condition at the pool surface, the coordinate transformation from $(s,\tau)$ to $(x,t)$ through the relation $x=X_c(s,\tau)$ and $t=\tau$ is performed. Considering the kinematic conditions (3.1*a*,*b*) and (3.1*c*,*d*), the chain rule yields

$$\frac{\partial}{\partial s}=\cos\theta\frac{\partial}{\partial x}, \quad \frac{\partial}{\partial \tau}=\frac{\partial}{\partial t}+(u_c\cos\theta-w_c\sin\theta)\frac{\partial}{\partial x}, \tag{3.11}$$

where the left-hand equation is the differentiation with respect to the variables expressed in terms of the coordinates $(s,\tau)$, and the right-hand equation, that with respect to the variables expressed in terms of the coordinates $(x,t)$.

In the following, the governing equations (3.9*a*)–(3.9*c*) are arranged so that the time evolution equations for the unkown variables, i.e. $H$, $u$, $w_c$ and $Z_c$, are derived. First,

https://doi.org/10.1017/jfm.2013.672 Published online by Cambridge University Press

the evolution equation for $Z_c$ is obtained; secondly, the equation to determine $u_c$ is determined; and finally, the continuity and momentum equations are presented in an evolutionary form.

Applying the chain rule (3.11) to $\partial\theta/\partial s$ and $\partial Z_c/\partial\tau$, we have

$$\frac{\partial\theta}{\partial s} = \frac{\partial^2 Z_c}{\partial x^2}\cos^3\theta, \tag{3.12a}$$

$$\frac{\partial Z_c}{\partial\tau} = \frac{\partial Z_c}{\partial t} + (u_c\cos\theta - w_c\sin\theta)\frac{\partial Z_c}{\partial x}, \tag{3.12b}$$

where $\partial\theta/\partial x$ has been calculated from the geometric relations:

$$\cos\theta = \frac{1}{\sqrt{1+(\partial Z_c/\partial x)^2}}, \quad \sin\theta = \frac{\partial Z_c/\partial x}{\sqrt{1+(\partial Z_c/\partial x)^2}}. \tag{3.13}$$

Comparing (3.12*b*) with (3.1*d*), we have the evolution equation for $Z_c$ as follows:

$$\frac{\partial Z_c}{\partial t} = \frac{w_c}{\cos\theta}, \tag{3.14}$$

while noting that $\partial Z_c/\partial x = \tan\theta$. Moreover, (3.3*a*) reduces to

$$\frac{\partial u_c}{\partial x} = w_c\frac{\partial^2 Z_c}{\partial x^2}\cos^2\theta, \tag{3.15}$$

which determines $u_c$.

Next, the chain rule (3.11) is applied to the governing equations (3.9*a*)–(3.9*c*), and the resultant equations are arranged to describe the time-evolution equations for $H$, $u$, and $w_c$ as follows;

$$\frac{\partial H}{\partial t} = -(u_c\cos\theta - w_c\sin\theta)\frac{\partial H}{\partial x} - \left(u\frac{\partial H}{\partial x} + H\frac{\partial u}{\partial x}\right)\cos\theta, \tag{3.16a}$$

$$\frac{\partial u}{\partial t} + \frac{\partial u_c}{\partial t} = -(u_c\cos\theta - w_c\sin\theta)\frac{\partial u}{\partial x} + \left(g - u\frac{\partial u}{\partial x}\right)\cos\theta, \tag{3.16b}$$

$$\frac{\partial w_c}{\partial t} = -2u\frac{\partial w_c}{\partial x}\cos\theta - \left\{-\frac{2\gamma}{\rho H} + u(u+2u_c)\right\}\frac{\partial^2 Z_c}{\partial x^2}\cos^3\theta - g\sin\theta. \tag{3.16c}$$

Thus finally, we have the fundamental equations of the liquid curtain, (3.14), (3.15), (3.16*a*), (3.16*b*) and (3.16*c*), for five unknowns $Z_c$, $u_c$, $H$, $u$ and $w_c$. The boundary conditions are given by (3.10*a*) and (3.10*b*).

Because the scaling applied in the above derivation does not restrict the magnitude of the slope of the liquid curtain, (3.16*a*)–(3.16*c*) are applicable for large-amplitude oscillations of the liquid curtain. The assumption that $u_c$ and $w_c$ are one order smaller than $u$ is reasonable from the experimental results presented in § 2.2.2.

In the case of a steady flow, the governing equations reduce to

$$u\frac{\partial H}{\partial x} + H\frac{\partial u}{\partial x} = 0, \tag{3.17a}$$

$$g - u\frac{\partial u}{\partial x} = 0, \tag{3.17b}$$

$$-g\sin\theta - \left(-\frac{2\gamma}{\rho H} + u^2\right)\frac{\partial^2 Z_c}{\partial x^2}\cos^3\theta = 0, \tag{3.17c}$$

https://doi.org/10.1017/jfm.2013.672 Published online by Cambridge University Press

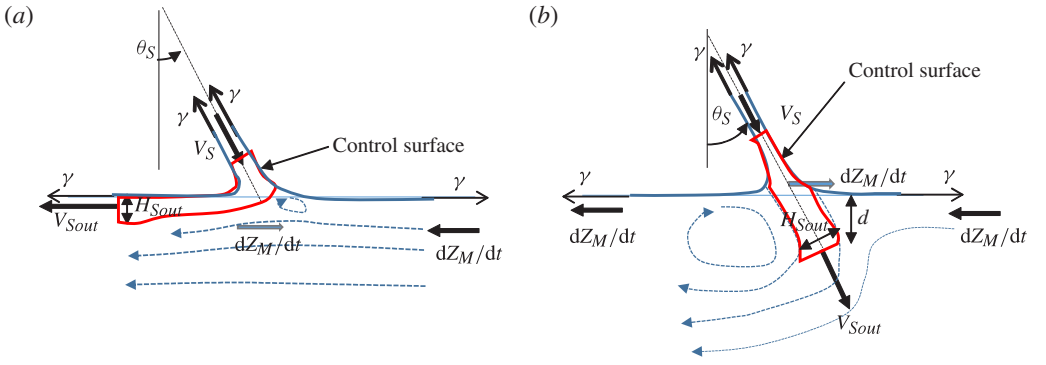



FIGURE 8. (Colour online) Control volume of oblique flow for (*a*) flow pattern I and (*b*) flow pattern II, where $z = Z_M$ denotes the position of the meniscus, $H_{Sout}$ and $V_{Sout}$ respectively denote the jet width and velocity at the exit of the jet from the control volume, and $d$ denotes the penetration depth of the jet in the pool for flow pattern II.

because $u_c = 0$ and $w_c = 0$ for steady flow. We note that the above equation coincides with the equation derived by Finnicum *et al.* (1993) because $\partial(\sin\theta)/\partial x = \partial^2 Z_c/\partial x^2 \cos^3\theta$ from (3.13).

In the case of small-amplitude oscillations of the liquid curtain, (3.14), (3.13) and (3.15) yield the following approximations:

$$w_c \approx \partial Z_c/\partial t, \quad u_c \approx 0, \quad \cos\theta \approx 1, \quad \sin\theta \approx \partial Z_c/\partial x, \tag{3.18}$$

and consequently, the governing equations yield

$$\frac{\partial H}{\partial t} = -\left(u\frac{\partial H}{\partial x} + H\frac{\partial u}{\partial x}\right), \tag{3.19a}$$

$$\frac{\partial u}{\partial t} = g - u\frac{\partial u}{\partial x}, \tag{3.19b}$$

$$\frac{\partial^2 Z_c}{\partial t^2} = -g\frac{\partial Z_c}{\partial x} - 2u\frac{\partial^2 Z_c}{\partial x \partial t} - \left(-\frac{2\gamma}{\rho H} + u^2\right)\frac{\partial^2 Z_c}{\partial x^2}. \tag{3.19c}$$

Equation (3.19*c*) can be written as

$$\rho H\left(\frac{\partial}{\partial t} + u\frac{\partial}{\partial x}\right)^2 Z_c = 2\gamma\frac{\partial^2 Z_c}{\partial x^2}, \tag{3.19d}$$

where (3.19*b*) has been considered. This equation is used in § 5.1 to study the linear response analysis of the liquid curtain to forced oscillations.

### 3.2. *Equations of meniscus motion*

Figure 8(*a,b*) shows schematics of two flow patterns observed in our experiment. In figure 8(*a*), the jet from the curtain attaches to the meniscus surface and deflects from $\theta = \theta_S$ to $\theta = -90°$. In contrast, in figure 8(*b*), the jet does not deflect in the meniscus and directly enters the pool. The flow velocities observed in the frame of reference moving at the same speed as the meniscus $dZ_M/dt$ are schematically shown, where $Z_M$ denotes the position of the meniscus.

https://doi.org/10.1017/jfm.2013.672 Published online by Cambridge University Press

3.2.1. *Derivation of the equation*

As shown in figure 6, the meniscus moves at a nearly constant speed. Therefore, the momentum conservation law is established in a frame of reference moving with the meniscus, and the dynamic equation of the meniscus is obtained. Figure 8(*a,b*) shows the control volume in which the momentum conservation law is applied. The boundary of the control volume is formed by the streamlines where the momentum flux is zero, the cross-section of the liquid curtain, and the outflow boundary of the jet where entrainment of liquid in the pool has not occurred.

When the Coanda effect is operative, the reaction force of the jet and the drag from the pool liquid act dominantly on the meniscus. However, when the Coanda effect ceases to act, the meniscus decelerates rapidly and stops, and then moves to a position directly under the slot. We derive the bulk equations describing the motion of the meniscus in the following section.

Initially, the external forces acting when the Coanda effect is operative are the surface tension from the liquid curtain, the momentum change in the liquid flowing through the meniscus, and the drag from the liquid in the pool induced by the motion of the meniscus. Hence, the equation describing the motion of the meniscus is given by

$$\rho S_M \frac{\mathrm{d}^2 Z_M}{\mathrm{d}t^2} = (\rho q V_S - 2\gamma)\sin\theta_S + \mathrm{sign}(\theta_S)\rho q V_{Sout} - C_d \frac{\rho H_{Sout}}{2}\left|\frac{\mathrm{d}Z_M}{\mathrm{d}t}\right|\frac{\mathrm{d}Z_M}{\mathrm{d}t}. \tag{3.20}$$

The left-hand side of (3.20) represents the inertia of the meniscus, where $S_M$ denotes the area of the meniscus. The first term on the right-hand side represents the momentum influx and the surface tension force from the liquid curtain, the second term represents the momentum outflux of the jet, whose sign changes according to the slope of the liquid curtain at the pool surface and the last term represents the drag induced by the movement of the meniscus; $H_{Sout}$ and $V_{Sout}$ respectively denote the width and velocity of the jet, and $C_d$ denotes the drag coefficient. Here, the entrainment of the pool liquid into the jet has been ignored; in other words, we select the control volume such that the entrainment is negligible. Consequently, the continuity of the unit discharge is expressed as follows:

$$q = H_S V_S = H_{Sout} V_{Sout}. \tag{3.21}$$

The speed of the meniscus directly under the slot is estimated from (3.20) as follows:

$$\frac{\mathrm{d}Z_M}{\mathrm{d}t} \approx \sqrt{\frac{2}{C_d}} V_{Sout}. \tag{3.22}$$

It is to be noted that the acceleration of the meniscus at the position immediately under the slot is zero because of the symmetry of the meniscus motion. Equation (3.22) indicates that the jet velocity $V_{Sout}$ and the speed of the meniscus $\mathrm{d}Z_M/\mathrm{d}t$ have the same order of magnitude.

Next, we derive the equation describing the motion of the meniscus when the Coanda effect ceases to act and the flow from the liquid curtain penetrates the pool surface. The momentum conservation law leads to the following equation of motion for the meniscus:

$$\rho S_M \frac{\mathrm{d}^2 Z_M}{\mathrm{d}t^2} = (\rho q V_S - 2\gamma)\sin\theta_S - \rho q V_{Sout}\sin\theta_{Sout} - C_d \frac{\rho d}{2}\left|\frac{\mathrm{d}Z_M}{\mathrm{d}t}\right|\frac{\mathrm{d}Z_M}{\mathrm{d}t}, \tag{3.23}$$

https://doi.org/10.1017/jfm.2013.672 Published online by Cambridge University Press

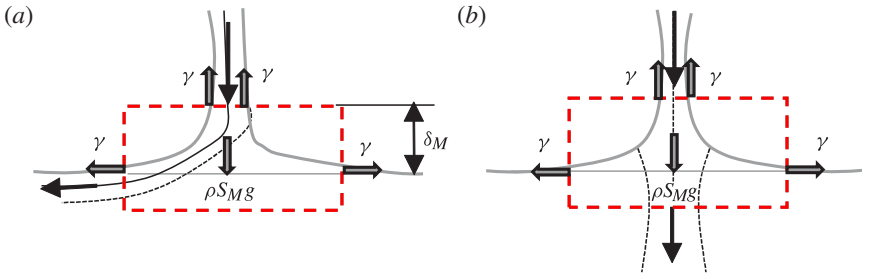



FIGURE 9. (Colour online) Schematic view of the scale of the meniscus for (*a*) flow pattern I and (*b*) flow pattern II. Here, the broken line indicates the boundary of the meniscus.

where $d$ denotes the penetration depth of the jet (see figure 8*b*), which is proportional to the jet momentum and inversely proportional to the square of the meniscus speed (Haniu & Ramaprian 1989). Therefore, we write

$$d = \eta \frac{qV_{Sout}}{(\mathrm{d}Z_M/\mathrm{d}t)^2}, \tag{3.24}$$

where $\eta$ denotes a non-dimensional parameter related to the jet length in the pool.

Substitution of (3.24) into (3.23) leads to

$$\rho S_M \frac{\mathrm{d}^2 Z_M}{\mathrm{d}t^2} = (\rho q V_S - 2\gamma)\sin\theta_S - \rho q V_{Sout}\sin\theta_S - C_d \frac{\eta}{2}\rho q V_{Sout}\mathrm{sign}\left(\frac{\mathrm{d}Z_M}{\mathrm{d}t}\right), \tag{3.25}$$

where we have assumed $\theta_{Sout} \approx \theta_S$ because the boundary of the control surface is chosen as the point immediately below the layer where the jet from the liquid curtain passes the meniscus.

As discussed in the introduction, the vortical structures around the jet in the pool are different from that of a solid body (Fric & Roshko 1994). The value of $C_d$ is also different from that for a two-dimensional solid body. However, since this problem is beyond our scope, $C_d$ is set to 1 in the present study.

### 3.2.2. *Scale of the meniscus*

The area $S_M$ of the meniscus, which appears in the momentum equation (3.20) and (3.25) is roughly estimated by the square of the capillary length. In the present section, we show that the area $S_M$ depends on the flow patterns.

Figure 9 shows the momentum balance in the vertical direction for flow patterns I and II. Consequently, the momentum balance for steady flow is given as follows:

$$\rho S_M g = \begin{cases} 2\gamma - \rho q V_S & \text{in I,} \\ 2\gamma - \rho q V_S + \rho q V_{Sout} & \text{in II.} \end{cases} \tag{3.26}$$

Equation (3.26) indicates that the meniscus of flow pattern I is smaller than that of flow pattern II, and the meniscus disappears when $\rho q V_S \geqslant 2\gamma$. From (3.26), $S_M$ can be expressed as

$$S_M = \begin{cases} \alpha \dfrac{2\gamma - \rho q V_S}{\rho g} & \text{in I,} \\ \alpha \dfrac{2\gamma - \rho q V_S + \rho q V_{Sout}}{\rho g} & \text{in II,} \end{cases} \tag{3.27}$$

https://doi.org/10.1017/jfm.2013.672 Published online by Cambridge University Press

where $\alpha$ denotes a zero-dimensional parameter related to the mass of the meniscus. The above equation shows that the necessary condition for the existence of the meniscus in flow pattern I is $We < 2$.

## 4. Numerical analysis

This section describes a numerical simulation of the steady and oscillatory oblique flows that is performed using the model derived in the previous section.

### 4.1. *Steady oblique flow*

A steady oblique flow occurs when $We_S \approx 1.2$–$1.6$ (see figure 3), and the solution satisfies

$$(2 - We_S)\sin\theta_S - \chi We_S = 0,\ \chi \equiv \frac{V_{Sout}}{V_S} \tag{4.1}$$

which follows from the momentum conservation law (3.20). Equation (4.1) yields the boundary condition of the curtain (3.17*c*) at the matching point between the curtain and the meniscus, that is

$$\sin\theta_S = \frac{\chi We_S}{2 - We_S} = \left.\frac{\partial Z_c/\partial x}{\sqrt{1 + (\partial Z_c/\partial x)^2}}\right|_{x=x_S}. \tag{4.2}$$

Here, we have ignored the scale of the meniscus. In figure 4, the curtain profiles calculated from $q = 0.623$ cm$^2$ s$^{-1}$, $\chi = 0.20$ and $q = 0.751$ cm$^2$ s$^{-1}$, $\chi = 0.28$ are manually superimposed on the corresponding experimental images. The value of $\chi$ is obtained from the experimental data of $\chi_{ex}$ given in table 3.

### 4.2. *Oscillatory oblique flow*

Figure 2(*c*) depicts the curtain and meniscus motions for an oscillatory oblique flow. These motions are simulated according to the following procedure.

① → ② Meniscus moves to the right as described by (3.20) owing to the reaction force from the jet emitted from the left as a result of the Coanda effect.

② → ③ The jet detaches from the meniscus surface when $\theta_S$ exceeds the detached angle $\theta_{det}$ and moves as described by (3.25).

③ → ④ When $\theta_S$ equals the attached angle $-\theta_{ata}$, the Coanda effect is again operational, and the meniscus moves to the left as described by (3.20).

Here, $\theta_{det}, \theta_{ata} \geqslant 0$, and the above processes are repeated in the numerical simulations. Moreover, the value of $\chi$ is fixed as a constant and is assumed to be similar to that of the steady oblique flow. We discuss $\chi$ later in § 5.4.

The curtain and the meniscus motions are coupled to each other upon imposing the following matching condition:

$$Z_c(x_S, t) = Z_M(t), \quad u(x_S, t) + u_c(x_S, t) = V_S(t). \tag{4.3}$$

The first and second conditions in (4.3) respectively express the continuity of the displacement and the flow velocity.

We apply a finite-difference scheme for the $x$-derivatives in (3.15) and (3.16*a*)–(3.16*c*), and then solve the resulting ordinary differential equations of $t$ numerically. Here, the $x$-derivatives of $Z_c$ are discretized by the centre-difference

https://doi.org/10.1017/jfm.2013.672 Published online by Cambridge University Press

scheme, and those of $H$, $u$, $u_c$, and $w_c$ are discretized by the forward-difference scheme.

Let $f_n = f(x_n)$, $x_n = (n-1)\Delta x$, $x_1 = 0$, and $x_N = x_S$ for any function $f$. By applying the finite-difference scheme to (3.15) and (3.16*a*)–(3.16*c*) and setting $n = 2, 3, \ldots, N-1$, we obtain a system of second-order ordinary differential equations for the unknowns $Z_{cn}$, $H_n$, $u_n$, $u_{cn}$, and $w_{cn}$ with $n = 2, 3, \ldots, N-1$. It is to be noted that $Z_{c1} = 0$, $H_1 = H_I$, $u_1 = V_I$, $u_{c1} = 0$, and $w_{c1} = 0$ because of the boundary condition (3.10*a*). The unknown $Z_{cN}$ is determined from (3.20) or (3.25) because of the boundary condition (4.3). The values of $Z_{c-1}$ and $Z_{cN+1}$ are extrapolated from the values at the adjacent mesh points.

Figure 10 depicts numerical simulations of the meniscus displacements and curtain profiles for $q = 1.20$ cm$^2$ s$^{-1}$ with $x_S = 1.85$ cm and $q = 1.13$ cm$^2$ s$^{-1}$ with $x_S = 2.5$ cm for various values of $\theta_{det}$ and $\theta_{ata}$. Here, $\chi$ is selected to satisfy $\chi = \chi_{cr}$, where

$$We_{cr} = \frac{2\sin\theta_{det}}{\sin\theta_{det} + \chi_{cr}}, \quad We_{cr} = 1.6, \tag{4.4}$$

so that the steady oblique flow does not exist when $We_S > 1.6$. Numerical simulations for $\theta_{ata} = 0$ show that the model developed in the present study reproduces the oscillatory behaviour of the liquid curtain, that is, the detachment and attachment of the jet around the meniscus causes an oscillatory oblique flow. Here, the assumption $\theta_{ata} = 0$ means that the Coanda effect becomes operational when the liquid curtain becomes vertical at the pool surface. As $\theta_{det}$ decreases, the amplitude reduces and the time interval for which the Coanda effect is inoperative becomes longer; as a result, the period of oscillations is too long compared to the experimental values, i.e. $A_{ex} = 8.9$ mm, $T_{ex} = 0.37$ s for $q = 1.13$ cm$^2$ s$^{-1}$ with $x_S = 2.5$ cm and $A_{ex} = 8.0$ mm, $T_{ex} = 0.57$ s for $q = 1.20$ cm$^2$ s$^{-1}$ with $x_S = 1.85$ cm, as listed in table 4.

The last row in figures 10(*a*) and 10(*b*) shows numerical results for $\theta_{det} = \theta_{ata}$, which indicates that the time when the Coanda effect is not operational is zero. Here, $\theta_{det} = 40^\circ$ in figure 10(*a*) and $\theta_{det} = 50^\circ$ in figure 10(*b*), which are considered to be reasonable from the experimental results (see figure 5). Subsequently, the period of oscillations and the amplitude approach the experimental value. Therefore, the reattachment mechanism of the jet needs to be investigated further, and a more elaborate model is required in order to predict the period of the oscillatory oblique flow.

We performed many numerical simulations for various values of the parameters $\alpha$, $\eta$, and $\theta_{det}$. For example, when $\alpha$ increases, the amplitude of oscillations increases; in the case of $\eta \geqslant 0.1$, the liquid curtain becomes nearly vertical, and then the oscillatory motion of the meniscus does not occur in the case of $\theta_{ata} = 0$.

## 5. Discussion

The undetermined parameters $\alpha$, $\eta$, and $\chi$ are dimensionless, and they are expected to be of the order of unity. The velocity ratio $\chi$ is around 0.3 for a steady oblique flow; however, it is unclear whether the velocity ratio depends on the meniscus velocity $\mathrm{d}Z_M/\mathrm{d}t$. Further, the values of $\theta_{det}$ and $\theta_{ata}$ depend on the Reynolds number of the flow in the meniscus. We discuss these problems in the following subsections.

### 5.1. *Period of oscillatory oblique flow*

The results of the numerical simulation described in § 4.2 indicate that the value of $\alpha$ affects the frequency of the oscillatory oblique flow. Herein, we show that the

https://doi.org/10.1017/jfm.2013.672 Published online by Cambridge University Press

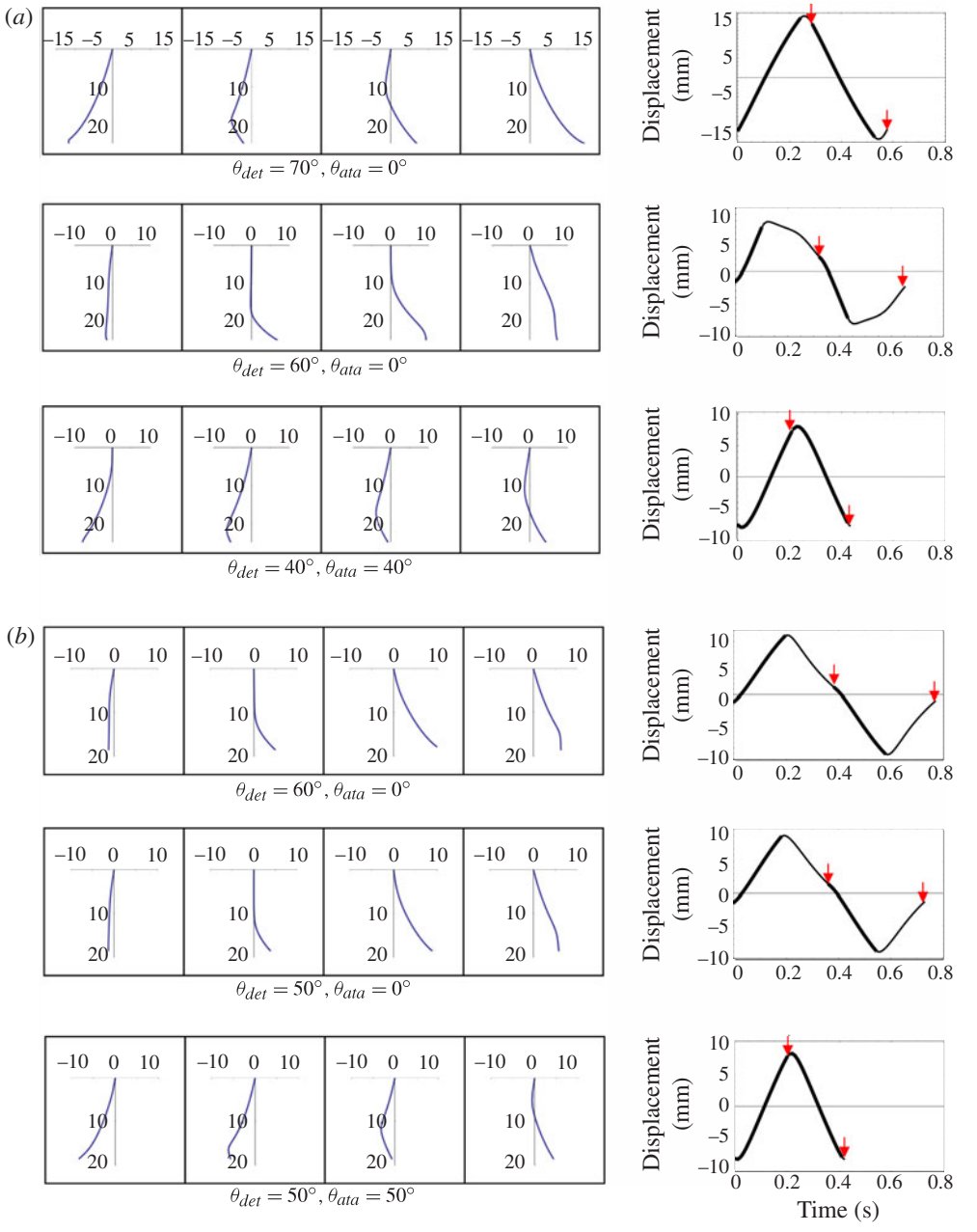



FIGURE 10. (Colour online) Curtain profile and meniscus displacement for (*a*) $q = 1.13$ cm$^2$ s$^{-1}$, $x_S = 2.5$ cm ($\alpha = 2$, $\chi = \chi_{cr}$, $\kappa = 0.04$, $C_d = 1$); and (*b*) $q = 1.20$ cm$^2$ s$^{-1}$, $x_S = 1.85$ cm ($\alpha = 2$, $\chi = \chi_{cr}$, $\kappa = 0.04$, $C_d = 1$). The left-hand plots depict the curtain profile, with time increasing from left to right, for various $\theta_{det}$ and $\theta_{ata}$ values as shown. The unit of length is one millimetre. The graphs on the right show the meniscus displacement. Thick and thin solid curves indicate the instances at which the Coanda effect is operative and inoperative, respectively. The arrows indicate the time at which the Coanda effect becomes operational.

https://doi.org/10.1017/jfm.2013.672 Published online by Cambridge University Press

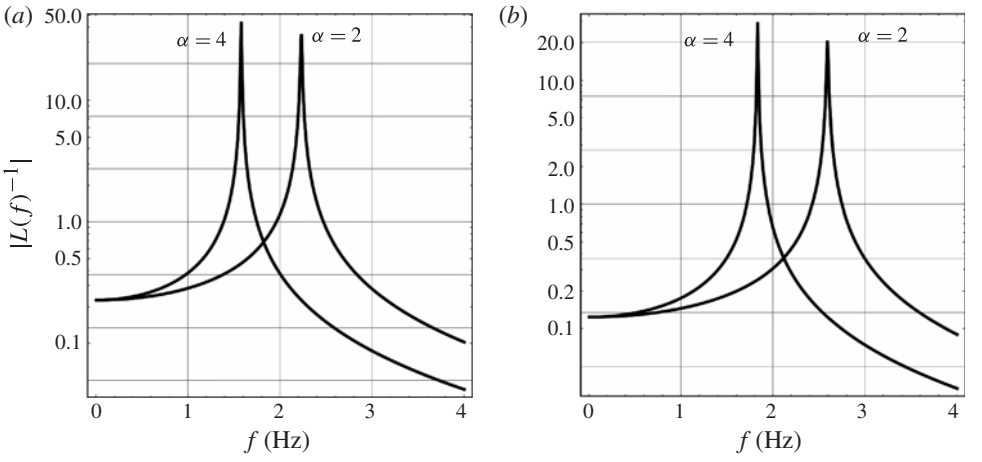



FIGURE 11. Magnitude of the linear response function $L(f)^{-1}$.
(*a*) $q = 1.13$ cm$^2$ s$^{-1}$, $x_S = 2.5$ cm. (*b*) $q = 1.120$ cm$^2$ s$^{-1}$, $x_S = 1.85$ cm.

frequency is roughly equal to the resonant frequency of the curtain, which is obtained from the most amplified mode in the linearized equations of motion.

The fundamental equations used are (3.19*d*), and the solution of (3.19*a*) and (3.19*b*):

$$u = \sqrt{u_I^2 + 2gx}, \quad u_I = \sqrt{u_0^2 - 4\left(\frac{4\mu g}{\rho}\right)^{2/3}}, \quad H = \frac{q}{u}. \tag{5.1}$$

Here, $u_0$ denotes the mean velocity at the die exit, $u_I$ denotes the liquid velocity implemented for a viscous liquid to consider the viscous stress at the die exit (Weinstein *et al.* 1997). The boundary conditions used are

$$Z_c|_{x=x_S} = Z_M, \quad \rho S_M \frac{\mathrm{d}^2 Z_M}{\mathrm{d}t^2} - (\rho q V_S - 2\gamma)\left.\frac{\partial Z_c}{\partial x}\right|_{x=x_S} = F(t), \tag{5.2}$$

where $F(t)$ represents the force exerted on the meniscus by the liquid in a pool, and it varies periodically with time owing to the occurrence and disappearance of the Coanda effect.

The boundary conditions for (3.19*d*) are $Z_c = 0$ at $x = 0$ and $Z_c = Z_S$ at $x = x_S$. Assuming periodic motions of the meniscus, the solution is set as $Z_c = \hat{Z}_c(x, f)\exp(2\pi \mathrm{i} f t)$, where i denotes the imaginary unit and $f$ denotes the frequency of oscillations. Upon substitution of the decomposition into (3.19*d*) and (5.2), the solution becomes

$$\hat{Z}_c(x, f) = \hat{F}(f)\hat{G}(x, f)L(f)^{-1}, \tag{5.3a}$$

$$L(f) \equiv -\rho S_M (2\pi f)^2 - (\rho q V_S - 2\gamma)\frac{\mathrm{d}\hat{G}}{\mathrm{d}x}(x_S, f), \tag{5.3b}$$

where $\hat{G}(x, f)\exp(2\pi \mathrm{i} f t)$ is the solution of (3.19*d*) under the boundary conditions $\hat{G}(0, f) = 0$ and $\hat{G}(x_S, f) = 1$. Figure 11 depicts the magnitude of the response function $L(f)^{-1}$. The peak is attained at around $f \approx 2$–$3$ Hz for $\alpha \approx 2$, which is nearly equal to the frequency of oscillations that can be observed in figure 6. Here, the value $\alpha \approx 2$ is reasonable since $\rho S_M$ includes the added mass of the meniscus.

https://doi.org/10.1017/jfm.2013.672 Published online by Cambridge University Press

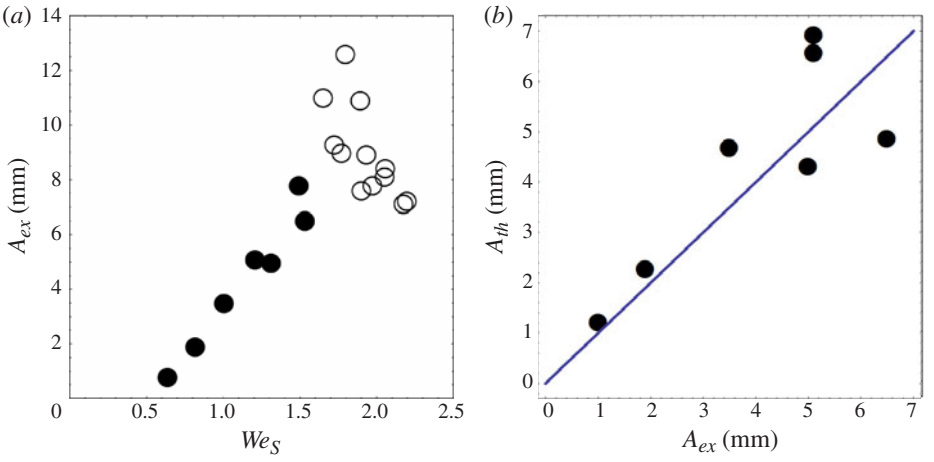



FIGURE 12. (Colour online) Amplitude of the meniscus displacement for oblique flows. (*a*) Weber number $We_S$ versus amplitude $A_{ex}$: ●, steady flow; ○, oscillatory flow. (*b*) Experimental value $A_{ex}$ versus theoretical prediction $A_{th}$.

### 5.2. *Amplitude of oblique flows*

Figure 12(*a*) shows the amplitude of the meniscus displacement for both steady and oscillatory oblique flows, as recorded in tables 3 and 4, as a function of $We_S$. The amplitude for oblique flow increases gradually as a function of $We_S$ until $We_S \approx 1.7$, and subsequently decreases up to $We_S \approx 2.3$, when the flow regime changes from oblique flow to steady jet.

Figure 12(*b*) shows the cross-plot of the amplitude of the meniscus displacement for a steady oblique flow, where the abscissa represents the experimental value $A_{ex}$ and the ordinate represents the theoretical value $A_{th}$ predicted from (3.17*a*)–(3.17*c*) and (4.2) for $\chi = \chi_{ex}$ in table 3. The theoretical values are strongly influenced by the value of $\chi_{ex}$ because of the boundary condition (4.2). The reason for this discrepancy is considered to originate from the accuracy of $\chi_{ex}$ which is determined from the velocity measurements in the experiment.

To investigate the amplitude of the liquid curtain for oscillatory oblique flows, the curtain profiles under the boundary conditions $Z_c = 0$ at $x = 0$ and $Z_c = A\sin(2\pi t/T)$ at $x = x_S$ are numerically simulated. Figure 13 shows the numerical result for the case of (*a*) $q = 1.13$ cm$^2$ s$^{-1}$ with $x_S = 2.5$ cm and of (*b*) $q = 1.20$ cm$^2$ s$^{-1}$ with $x_S = 1.85$ cm. Here, the period $T$ and amplitude $A$ are taken from the experimental data. The maximum value of $\theta_S$ for each flow is (*a*) 40° and (*b*) 50°. Moreover, the curtain profile in figure 13 is similar to that in figure 10 even when the boundary conditions are different. This implies that the mechanism of oscillations induced by the Coanda effect enhances the forced oscillations of the liquid curtain; for instance, the angle $\theta_S$ immediately under the slot is positive when $\mathrm{d}Z_S/\mathrm{d}t > 0$ and vice versa.

### 5.3. *Detachment angle* $\theta_{det}$

Oblique flow occurs because of the deflection of the two-dimensional jet in the meniscus. Jet deflection around a circular cylinder has been previously studied by Newman (1961). He showed that the deflection angle depends on the ratio between the jet width and cylinder radius and the Reynolds number defined by the jet momentum and viscosity. In the present study, the jet width is denoted by $H_S$ and the

https://doi.org/10.1017/jfm.2013.672 Published online by Cambridge University Press

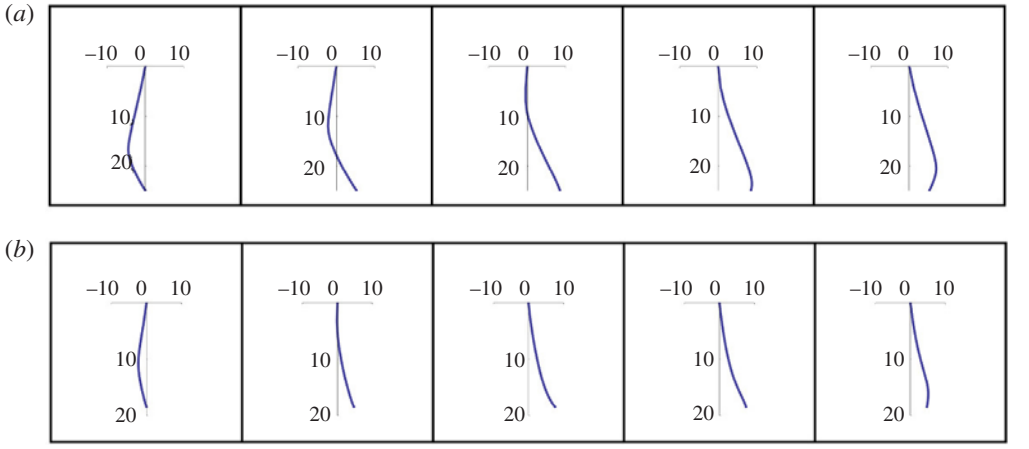



FIGURE 13. (Colour online) Curtain profiles for the forced oscillations $Z_S = A\sin(2\pi t/T)$. Here, for (*a*) $q = 1.13$ cm$^2$ s$^{-1}$ with $x_S = 2.5$ cm and a period of 0.37 s, and $A = 8.9$ mm and for (*b*), $q = 1.20$ cm$^2$ s$^{-1}$ with $x_S = 1.85$ cm and a period of 0.57 s, and $A = 8.0$ mm. The maximum value of $\theta_S$ here is (*a*) 40° and (*b*) 50°.

cylinder radius is replaced by a meniscus with a height denoted by $\delta_M$, and hence, the deflection angle $\Delta\theta$ is expressed as

$$\Delta\theta = \Phi\left[\frac{H_S}{\delta_M}, Re_M\right], \tag{5.4a}$$

$$Re_M \equiv \frac{\rho V_S H_S}{\mu}\sqrt{\frac{\delta_M}{H_S}}, \quad \delta_M = \sqrt{2 - We_S}\sqrt{\frac{\gamma}{\rho g}}, \tag{5.4b}$$

where $Re_M$ denotes the Reynolds number introduced by Newman (1961), and $\delta_M$ is roughly approximated as $\sqrt{S_M}$, where $S_M$ is obtained from (3.27) for flow pattern I. Since $\delta_M/H_S \sim O(1\ \text{mm}/100\ \mu\text{m}) = O(10)$ in the present experiments, the range of $Re_M$ for which the Coanda effect is operative is roughly 200–500. Moreover, in the case when $H_S \ll \delta_M$, $\Delta\theta$ depends only on $Re_M$. The deflection angle for oblique flows is at least greater than 100°, as can be seen in figure 4, and increases up to around 160°, as can be seen in figure 5. Although a limited amount of experimental data are available for a flow with a low Reynolds number of a few hundreds, the deflection angle for the flow around the meniscus is nearly equal to that in the circular cylinder experiment (Fekete 1963).

The value of the deflection angle for the meniscus in the present experiment cannot be compared directly with the value in the cylinder experiment, because the physical conditions surrounding the flow phenomena in each case are different, as follows. First, the jet in the meniscus is in a free shear flow over a free surface so that the momentum diffusion is suppressed compared with that for a jet over a solid boundary. Second, there is a pressure gradient in the meniscus along the horizontal direction for oblique flows because of the difference in the curvatures between the left- and right-hand sides of the meniscus.

### 5.4. *Velocity ratio* $\chi$

The experiment for the steady oblique flow shows that the flow velocity decays strongly immediately before and after the meniscus, and the value of the velocity

https://doi.org/10.1017/jfm.2013.672 Published online by Cambridge University Press

ratio $\chi$ dominates the curtain profile as indicated from (4.2). Hence, we discuss here the value selected for the velocity ratio $\chi$ by considering the spreading of a turbulent jet and the energy loss due to the bending of the jet in the meniscus.

A plane turbulent jet spreads downstream and the rate of spreading $\tilde{S}$ is around 0.1 (see Pope 2000); hence, the thickness of the jet varies from $H_S$ to $H_S + 0.1L$, where $L$ denotes the jet length. Since the jet length $L$ can be approximated by the meniscus length, i.e. $L \approx \delta_M$, the equation of continuity (3.21) for a steady flow leads to

$$V_{Sout} = \frac{H_S}{H_S + \tilde{S}\delta_M} V_S \approx 0.5 V_S. \tag{5.5}$$

Here, $H_S \approx 200$ μm, $\delta_M \approx 2000$ μm, and $\tilde{S} = 0.1$. Since $\tilde{S}$ is larger for a plane jet with a low Reynolds number over a curved surface (see Newman 1961; Neuendorf & Wygnanski 1999), the velocity ratio $\chi_{ex}$ becomes smaller than 0.5. Further, the momentum deficit of the jet occurs due to the bending of the jet in the meniscus. The kinetic energy of the jet lost because of the jet bending by 90° is around 10 % of the kinetic energy before the bending (see for instance Erwin & Idelchik 1989). Considering these two facts, the value $\chi \approx 0.3$ in the experiments seems to be reasonable.

Next, we show that velocity ratio $\chi$ for an oscillatory oblique flow is a decreasing function of the meniscus velocity $\dot{Z}_M \equiv \mathrm{d}Z_M/\mathrm{d}t$. For low-Reynolds-number flows, the rate of spreading $\tilde{S}$ depends on the Reynolds number $Re_M$, and $\partial\tilde{S}/\partial Re_M < 0$ (see Newman 1961). Moreover, the Reynolds number $Re_M$ for an oscillatory oblique flow is given by

$$Re_M \equiv \frac{\rho(V_S - \dot{Z}_M)H_S}{\mu}\sqrt{\frac{\delta_M}{H_S}}, \tag{5.6}$$

where $V_S$ in (5.4*b*) is replaced by $V_S - \dot{Z}_M$ because the diffusion of the jet depends on the relative flow velocity between the jet and the ambient flow. Considering (5.6) and $\chi \approx H_S/(H_S + \tilde{S}\delta_M)$ from (5.5), we have

$$\frac{\partial\chi}{\partial\dot{Z}_M} \approx \frac{H_S\delta_M}{(H_S + \tilde{S}\delta_M)^2}\frac{\rho H_S}{\mu}\sqrt{\frac{\delta_M}{H_S}}\frac{\partial\tilde{S}}{\partial Re_M} < 0, \tag{5.7}$$

that is, $\chi$ is a decreasing function of $\dot{Z}_M$. Hence, it is considered that the velocity ratio in oscillatory flows is smaller than that for a steady oblique flow.

## 6. Conclusions

A liquid curtain bridged between a slot exit and a pool surface has various flow regimes. They originate from the Coanda effect of the jet inside the meniscus formed between the curtain and the pool. The necessary condition for the Coanda effect to occur in the meniscus is that the jet width be less than the radius of curvature of the meniscus, and hence, the phenomena described in the study cannot be observed for a water curtain with thickness greater than a few milimetres.

The summary and conclusions of the study are as follows:

(i) Steady vertical flow, steady oblique flow, and oscillatory oblique flow are observed in the low-Weber-number flow of a liquid curtain bridged between two vertical edge guides and a pool surface.

https://doi.org/10.1017/jfm.2013.672 Published online by Cambridge University Press

(ii) These patterns are caused by the Coanda effect of the jet around the meniscus that is formed in the matching region common to the liquid curtain and the pool surface.

(iii) The equation describing the motion of the liquid curtain applicable for a finite curtain slope is obtained using the intrinsic coordinate system.

(iv) The equation of the meniscus motion is derived by considering the conservation of momentum in the control volume surrounding the meniscus.

(v) The curtain deformations in oblique flows are analysed by generating numerical simulations of these equations and are then compared with experimental results. The results show that both the period and the amplitude of the oscillations can be explained by the present model.

(vi) The period of oscillatory oblique flow is discussed and explained via the response analyses of the curtain, and the result shows that the period of the oscillations is close to that of the most amplified mode of the liquid curtain.

Further studies focusing on the following subjects are required:

(i) Coanda effect of the flow around the meniscus;

(ii) vortical structure in the wake of the jet in the pool.

**Acknowledgements**

This work was supported in part by a Grant-in-Aid for Scientific Research (A) 22248025 from JSPS (Principal Investigator; Professor Y. Adachi).

**Supplementary movies**

Supplementary movies are available at http://dx.doi.org/10.1017/jfm.2013.672.

**Appendix. Acceleration of a fluid particle in the framework of the centre-surface**

One of the referees for the present paper pointed out the validity of the governing equations shown in Ida (1995) and Ida & Miksis (1998). The same coordinate system has been used in van de Fliert *et al.* (1995), and Yao & Stewart (1996). Further, van de Fliert *et al.* (1995) introduced approximated equations for the small curvature of the centre-surface. Yao & Stewart (1996) designated this coordinate system as 'Betrand-intrinsic coordinates', and they obtained the relevant reduced governing equations, wherein the intermediate variable $\theta$ was not introduced, and hence, we cannot verify the validity of the governing equations obtained by Ida (1995) and Ida & Miksis (1998). Therefore, here, we re-derive the Euler equations of motion in the coordinate system introduced by Ida et al. following their ideas.

The acceleration of a fluid particle along the $x$- and $z$-directions in the Cartesian coordinate system is given respectively by

$$a_x \equiv \frac{\partial U}{\partial t} + U\frac{\partial U}{\partial x} + W\frac{\partial U}{\partial z}, \quad a_z \equiv \frac{\partial W}{\partial t} + U\frac{\partial W}{\partial x} + W\frac{\partial W}{\partial z}. \tag{A 1}$$

Consider the transformations of variables from $(x, z, t)$ to $(s, n, \tau)$ through the following functional relationships:

$$x = X_c(s, \tau) - n\sin\theta(s, \tau), \quad z = Z_c(s, \tau) - n\cos\theta(s, \tau), \quad t = \tau, \tag{A 2}$$

where $(X_c, Z_c)$ denotes the position vector on the centre-curve of the sheet, $s$ denotes the intrinsic coordinate along the centre-curve, $n$ denotes the coordinate normal to the

https://doi.org/10.1017/jfm.2013.672 Published online by Cambridge University Press

centre-curve, $\tau$ denotes the time in the frame of reference $(s, n)$, and $\theta$ represents an auxiliary variable defined by the following equations:

$$\frac{\partial X_c}{\partial s}(s,\tau)=\cos\theta(s,\tau),\qquad \frac{\partial Z_c}{\partial s}(s,\tau)=\sin\theta(s,\tau). \tag{A 3}$$

In order to describe the acceleration of a fluid particle by using its velocity along the $s$- and $n$-directions, the flow velocity $(u, w)$ and the centre-curve velocity $(u_c, w_c)$ in the frame of reference $(s, n)$ are introduced according to the following equations:

$$U(x,z,t)=u(s,n,\tau)\cos\theta(s,\tau)-w(s,n,\tau)\sin\theta(s,\tau), \tag{A 4a}$$
$$W(x,z,t)=u(s,n,\tau)\sin\theta(s,\tau)+w(s,n,\tau)\cos\theta(s,\tau), \tag{A 4b}$$
$$\frac{\partial X_c}{\partial \tau}(s,\tau)=u_c(s,\tau)\cos\theta(s,\tau)-w_c(s,\tau)\sin\theta(s,\tau), \tag{A 4c}$$
$$\frac{\partial Z_c}{\partial \tau}(s,\tau)=u_c(s,\tau)\sin\theta(s,\tau)+w_c(s,\tau)\cos\theta(s,\tau). \tag{A 4d}$$

Note that $(u_c, w_c)$ denotes the velocity vector of the centre-curve for a fixed value of $s$ in the $s$–$n$ coordinate system.

The derivatives of $s$ and $n$ with respect to $x$, $z$, and $t$ are obtained by differentiating (A 2) with respect to $x$, $z$, and $t$ as follows:

$$\frac{\partial s}{\partial x}=\frac{\cos\theta}{\ell},\quad \frac{\partial s}{\partial z}=\frac{\sin\theta}{\ell},\quad \frac{\partial s}{\partial t}=\frac{1}{\ell}\left(n\frac{\partial\theta}{\partial\tau}-u_c\right), \tag{A 5a}$$
$$\frac{\partial n}{\partial x}=-\sin\theta,\quad \frac{\partial n}{\partial z}=\cos\theta,\quad \frac{\partial n}{\partial t}=-w_c, \tag{A 5b}$$
$$\ell\equiv 1-n\frac{\partial\theta}{\partial s}, \tag{A 5c}$$

where (A 3), (A 4*c*) and (A 4*d*) have been used to simplify the above formulae. The above derivatives are used to transform (A 1) from the $x$–$z$ coordinate system to the $s$–$n$ coordinate system.

Substituting (A 4*a*) and (A 4*b*) into (A 1), applying the chain rule and using (A 5*a*)–(A 5*c*), the acceleration of the fluid particle along the $s$- and $n$-directions is given, respectively, as follows:

$$\begin{aligned} a_s &= a_x\cos\theta+a_z\sin\theta \\ &= \frac{\partial u}{\partial\tau}+(u-u_c)\frac{\partial u}{\ell\partial s}+(w-w_c)\frac{\partial u}{\partial n}-w(u-u_c)\frac{\partial\theta}{\ell\partial s}+\left(n\frac{\partial u}{\ell\partial s}-\frac{w}{\ell}\right)\frac{\partial\theta}{\partial\tau}, \end{aligned} \tag{A 6a}$$
$$\begin{aligned} a_n &= -a_x\sin\theta+a_z\cos\theta \\ &= \frac{\partial w}{\partial\tau}+(u-u_c)\frac{\partial w}{\ell\partial s}+(w-w_c)\frac{\partial w}{\partial n}+u(u-u_c)\frac{\partial\theta}{\ell\partial s}+\left(n\frac{\partial w}{\ell\partial s}+\frac{u}{\ell}\right)\frac{\partial\theta}{\partial\tau}. \end{aligned} \tag{A 6b}$$

The last term in (A 6*a*) and (A 6*b*) that is proportional to $n$ is absent in the equations derived in Ida (1995) and Ida & Miksis (1998). Defining the relative velocity $(u, w)$ as

$$u=u-u_c,\qquad w=w-w_c, \tag{A 7}$$

and substituting (A 7) into (A 6*a*) and (A 6*b*), the Euler equations of motion in the $s$–$n$ curvilinear coordinate system are obtained as shown in (3.2*b*) and (3.2*c*). Note that the velocity frame observed from the inertial coordinate system, $(u_c, w_c)$, is independent

https://doi.org/10.1017/jfm.2013.672 Published online by Cambridge University Press

of $n$, and the relative velocity $(u, v)$ is not the Lagrangian velocity, as shown below. Therefore, the present governing equations (3.2*a*)–(3.2*c*) are different from those based on the framework of the Cosserat rod theory (for instance, Ribe, Habibi & Bonn 2006; Arne *et al.* 2010).

To clarify the meaning of the relative velocity $(u, w)$, the fluid particle velocity in the $s$–$n$ coordinate system is calculated by setting $x = x(t)$ and $z = z(t)$ in (A 2) and differentiating (A 2) with respect to $t$ as follows:

$$\frac{\mathrm{d}x}{\mathrm{d}t} = u_c + \ell\frac{\mathrm{d}s}{\mathrm{d}t} - n\frac{\partial\theta}{\partial\tau}, \quad \frac{\mathrm{d}z}{\mathrm{d}t} = w_c + \frac{\mathrm{d}n}{\mathrm{d}t}, \quad \tau = t, \tag{A 8}$$

where the relations (A 3), (A 4*c*) and (A 4*d*) have been considered. Comparison between (A 7) and (A 8) indicates that the Euler–Lagrange relation, that is, the relation between the fluid particle velocity and the flow velocity, can be written as follows:

$$\ell\frac{\mathrm{d}s}{\mathrm{d}t} = u + n\frac{\partial\theta}{\partial\tau}, \quad \frac{\mathrm{d}n}{\mathrm{d}t} = w, \quad \tau = t, \tag{A 9}$$

which indicates that $u$ is not equal to the fluid particle velocity in the framework of the centre-curve. Applying the above relations, the kinematic boundary condition at the free surface, $n = h(s, \tau)$, is calculated as

$$\begin{aligned}\frac{\mathrm{d}}{\mathrm{d}t}(n - h(s,\tau)) &= \frac{\mathrm{d}n}{\mathrm{d}t} - \frac{\partial h}{\partial\tau} - \frac{\partial h}{\partial s}\frac{\mathrm{d}s}{\mathrm{d}t} \\ &= w - \frac{\partial h}{\partial\tau} - \frac{\partial h}{\ell\partial s}\left(u + n\frac{\partial\theta}{\partial\tau}\right),\end{aligned} \tag{A 10}$$

which leads to

$$w|_{n=h(s,\tau)} = \frac{\partial h}{\partial\tau} + \frac{\partial h}{\ell\partial s}\left(u + h\frac{\partial\theta}{\partial\tau}\right)\bigg|_{n=h(s,\tau)}. \tag{A 11}$$

## REFERENCES


ARNE, W., MARHEINEKE, N., MEISTER, A. & WEGENER, R. 2010 Numerical analysis of Cosserat rod and string models for viscous jets in rotational spinning processes. *Math. Models Meth. Appl. Sci.* **20** (10), 1941–1965.

ERWIN, F. & IDELCHIK, I. E. 1989 *Flow Resistance: a Design Guide for Engineers*. Hemisphere.

FEKETE, G. I. 1963 Coanda flow of a two-dimensional wall jet on the outside of a circular cylinder. *Tech. Rep. Mechanical Engineering Research Laboratories* 63–11. McGill University.

FINNICUM, D. S., WEINSTEIN, S. J. & RUSCHAK, K. J. 1993 The effect of applied pressure on the shape of a two-dimensional liquid curtain falling under the influence of gravity. *J. Fluid Mech.* **255**, 647–665.

VAN DE FLIERT, B. W., HOWELL, P. D. & OCKENDON, J. R. 1995 Pressure-driven flow of a thin viscous sheet. *J. Fluid Mech.* **292**, 359–376.

FRIC, T. F. & GHARIB, M. 1990 Wake formation of the transverse jet. *Bull. Am. Phys. Soc.* **35**, 2338–2347.

FRIC, T. F. & ROSHKO, A. 1994 Vortical structure in the wake of a transverse jet. *J. Fluid Mech.* **279**, 1–47.

HANIU, H. & RAMAPRIAN, B. R. 1989 Studies on two-dimensional curved nonbuoyant jets in cross flow. *Trans. ASME: J. Fluids Engng* **111** (1), 78–86.

HIGGINS, B. G. & SCRIVEN, L. E. 1979 Interfacial shape and evolution equations for liquid films and other viscocapillary flows. *Ind. Engng Chem. Fundam.* **18** (3), 208–215.


https://doi.org/10.1017/jfm.2013.672 Published online by Cambridge University Press

IDA, M. P. 1995 The dynamics of thin liquid films. PhD thesis, Northwestern University, Evanston.

IDA, M. P. & MIKSIS, M. J. 1998 The dynamics of thin films I: general theory. *SIAM J. Appl. Maths* **58** (2), 456–473.

KHESHGI, H. S., KISTLER, S. F. & SCRIVEN, L. E. 1992 Rising and falling film flows: Viewed from a first-order approximation. *Chem. Engng Sci.* **47–3**, 683–694.

KISTLER, S. F. 1984 The fluid mechanics of curtain coating and other related viscous free surface flows with contact lines. PhD thesis, University of Minnesota.

KISTLER, S. F. & SCHWEIZER, P. M. 1997 *Liquid Film Coating: Scientific Principles and their Technological Implications*. Kluwer.

KYOTOH, H., TSUDA, T., TAKAGI, M. & NAKANO, K. 2009 Momentum integral equation for an unsteady falling liquid curtain. *Kyoto University Research Information Repository* **1645**, 194–201 (in Japanese).

NEWMAN, B. G. 1961 The deflexion of plane jets by adjacent boundaries-coanda effect. In *Boundary Layer and Flow Control* (ed. G. V. Lachmann), pp. 232–264. Pergamon.

NEUENDORF, R. & WYGNANSKI, I. 1999 On a turbulent wall jet flowing over a circular cylinder. *J. Fluid Mech.* **381**, 1–25.

POPE, S. G. 2000 *Turbulent Flows*. Cambridge University Press.

RIBE, N. M., HABIBI, M. & BONN, D. 2006 Stability of liquid rope coiling. *Phys. Fluids* **18**, 084102.

SEBILLEAU, J., LIMAT, L. & EGGERS, J. 2009 Flow separation from a stationary meniscus. *J. Fluid Mech.* **633**, 137–145.

TAKAGI, M. 2010 Transfer of a falling liquid curtain to liquid or solid surfaces. Master's thesis, Graduate School of Systems and Information Engineering, University of Tsukuba (in Japanese).

WEINSTEIN, S. J., CLARKE, A., MOON, A. G. & SIMISTER, E. A. 1997 Time-dependent equations governing the shape of a two-dimensional liquid curtain, Part 1: Theory. *Phys. Fluids* **9**, 3625–3636.

WEINSTEIN, S. J., HOFF, J. W. & ROSS, D. S. 1998 Time-dependent equations governing the shape of a three-dimensional liquid curtain. *Phys. Fluids* **10**, 1815–1818.

YAO, J. & STEWART, D. S. 1996 Dynamics of multi-dimensional detonation. *J. Fluid Mech.* **309**, 225–275.

https://doi.org/10.1017/jfm.2013.672 Published online by Cambridge University Press